https://doi.org/10.5194/egusphere-2022-1099
Preprint. Discussion started: 18 October 2022

Effects of including the adjoint sea ice rheology on estimating Arctic ocean-sea ice state

Guokun Lyu[1], Armin Koehl[2], Xinrong Wu[3], Meng Zhou[1], and Detlef Stammer[2]

[1]Shanghai Key Laboratory of Polar Life and Environment Sciences, School of Oceanography, Shanghai Jiao Tong University, Shanghai, China

[2]Center for Earth System Research and Sustainability (CEN), University of Hamburg, Hamburg, Germany

[3]Key Laboratory of Marine Environmental Information Technology, National Marine Data and Information Service, Tianjin, China

Correspondence to: Guokun Lyu (guokun.lyu@sjtu.edu.cn)

Abstract. The adjoint technique has been applied to the coupled ocean and sea ice models for sensitivity studies and Arctic state estimation. However, the accuracy of the adjoint model is degraded by simplifications on the adjoint of the sea ice model, especially adjoint sea ice rheology. As part of ongoing developments of coupled ocean and sea ice estimation system, we incorporate and stabilize the adjoint of viscous-plastic sea ice dynamics (adjoint-VP) and compare it with the adjoint of a free drift sea ice model (adjoint-FD) through assimilation experiments. Using the adjoint-VP resulted in a further cost reduction of 7.9% in comparison to adjoint-FD with noticeable improvements in ocean temperature over the open water and intermediate layers of the Arctic Ocean. Adjoint-VP more efficiently adjusts uncertain parameters than adjoint-FD by involving different sea ice retreat processes. For instance, adjoint-FD melts sea ice up to 1.0 m in the marginal seas from May to June through over-adjusting air temperature (>8 ℃); adjoint-VP reproduces the sea ice retreat with smaller adjustments on the atmospheric state within the prior uncertainty range. The developments of the adjoint model here lay the foundation for further improving Arctic ocean and sea ice estimation through comprehensively adjusting the initial conditions, atmosphere forcings, and model parameters.

https://doi.org/10.5194/egusphere-2022-1099
Preprint. Discussion started: 18 October 2022

1 Introduction

The Arctic Ocean has experienced drastic changes and has been migrating to a new state over the past decades, concerning the fast declining sea ice (Comiso et al., 2008; Kwok, 2018), increased inventory of freshwater in the western Arctic (Proshutinsky et al., 2019), enhanced warm inflows from the Pacific Ocean (Woodgate et al., 2012) and the Atlantic Ocean (Polyakov et al., 2017; Quadfasel et al., 1991), and increased ocean primary productivity (AMAP, 2021). These changes amplify the local air and ocean temperature and potentially impact the climate and weather of the Northern Hemisphere (Ma et al., 2022; Overland et al., 2021).

Over the recent years, progress has been made in satellite techniques (e.g., Kaleschke et al., 2001; Spreen et al., 2008), in-situ observations (e.g., Toole et al., 2016; Morison et al., 2007; Polyakov et al., 2017; Proshutinsky et al., 2009; Schauer et al., 2008), and coupled ocean and sea ice models. However, the lack of extensive Arctic observations, especially direct observations of the state variables and fluxes through the water column, and deficiencies of the coupled ocean and sea-ice model still obscure our understanding of the Arctic sea-ice changes and extremes. Accurate predictions of sea ice is therefore also limited (e.g., Yang et al., 2020).

To fill the gaps, research groups have applied data assimilation techniques to ingest available observations into coupled ocean and sea ice models, reconstructing spatio-temporal changes of the Arctic Ocean. The resulting reanalyses are assumed to advance in fidelity since the development of models and data assimilation methods progress, and observation numbers increase, providing invaluable information for understanding the Arctic changes and the related ocean-atmosphere-ice heat and freshwater fluxes. Among the various data assimilation methods, an adjoint method with a large assimilation window (years to decades) has been developed within the framework of Estimating the Circulation and Climate of the Ocean (Heimbach et al., 2019; Stammer et al., 2002; Wunsch and Heimbach, 2007) to create a dynamically consistent synthesis, permitting closed budget analysis (e.g., Buckley et al., 2014; Piecuch and Ponte, 2012). Within the assimilation window, the adjoint method attempts to make the model simulation consistent with available observations iteratively by correcting model uncertain inputs (control variables hereafter), including initial conditions, atmospheric forcing, and model parameters to yield minimum misfits measured by an objective function. An adjoint model (adjoint of the tangent linear approximation of the nonlinear model) is used as a spatio-temporal interpolator to project the model-data misfits onto the gradient of a cost function with respect to the control variables. Therefore, the accuracy of the adjoint model is crucial for the performance of the miniation and ultimately the quality of the synthesis.

The adjoint method has been applied to the coupled ocean and sea ice system for adjoint sensitivities studies (Heimbach et al., 2010; Kauker et al., 2009; Koldunov et al., 2013) and Arctic synthesis (Fenty and Heimbach, 2013; Koldunov et al., 2017; Lyu et al., 2021b; Nguyen et al., 2021). However, due to the persistence of numerically instability issues, the adjoint of sea ice dynamics is omitted (Forget et al., 2015; Nguyen et al., 2021; Fenty and Heimbach, 2013; Mazloff et al., 2010) or simplified to a free-drift sea ice model (Koldunov et al., 2017; Lyu et al., 2021a; Lyu et al., 2021b). Toyoda et al. (2019) described stabilizing the adjoint of full elastic–viscous–plastic sea-ice dynamics and noted much weaker evolution of sensitivity to sea-ice velocity by O (10^2) in the central Arctic Ocean than the adjoint of free-drift sea ice dynamic. Therefore, using the adjoint of a free-drift sea ice dynamic may

https://doi.org/10.5194/egusphere-2022-1099
Preprint. Discussion started: 18 October 2022

overestimates the gradients of the cost function towards the sea-ice velocity and wind, which potentially impairs the usefulness of the adjoint gradients and hinders the minimization of the model-data misfits.

In this study, we incorporate and stabilize the adjoint of a viscous-plastic sea ice dynamic (Hibler 1979; Zhang and Hibler Iii, 1997), building on prior developments of the adjoint method in the Arctic Ocean (Fenty and Heimbach, 2013; Heimbach et al., 2010; Koldunov et al., 2017; Lyu et al., 2021b). Taking the unprecedented sea ice retreat process in 2012 as an example, we evaluate the impacts of using the adjoint of full sea ice dynamics on estimating the Arctic ocean and sea ice and sea-ice retreat processes.

The paper is organized as follows. In section 2, we introduce the model configurations and assimilation experiments. We assess the assimilation results in section 3 regarding the residual errors. We examine adjustments of the control variables in section 4 and compare sea ice retreat process from April 10, 2012 to September 20, 2012 in section 5. Section 6 summarizes the results of this study.

2 Model Configuration and Experiment Setups

2.1 The Coupled Ocean-Sea Ice Model and Assimilation System

The data assimilation system is based on the adjoint method in the framework of ECCO, using the Massachusetts Institute of Technology ocean general circulation model (MITgcm, Marshall et al., 1997) coupled with a zero-layer dynamic-thermodynamic sea ice model of Hibler (1979). The sea ice dynamics are based on the viscous-plastic rheology and are solved using a line successive over-relaxation algorithm (Zhang and Rothrock, 2000) and are modified to facilitate the generation of adjoint model (Losch et al., 2010). The adjoint of the coupled ocean and sea ice model is generated by the Transformation of Algorithms in FORTRAN (TAF, Giering and Kaminski, 1998).

The pan-Arctic model covers the Arctic Ocean north of the Bering Strait and the Atlantic Ocean 44° N (Figure 1). In the horizontal, we use a curvilinear grid with a resolution of 12~15 km in the Arctic Ocean and ~18 km in the north Atlantic Ocean. In the vertical, the system has 50 z-levels ranging from 10 m at the surface to 456 m in the deep ocean. The open boundaries are provided by a 16 km Atlantic-Arctic Ocean simulation (Serra et al., 2010). At the ocean surface, we use the atmosphere state from the National Centers for Environmental Prediction reanalysis 1 (NCEP-RA1, Kalnay et al., 1996) and bulk formulae to compute the momentum, heat, and freshwater fluxes. A virtual salt flux parameterization simulates the dilution and salinification of rainfall, evaporation, and river runoff. The river runoff is applied near the river mouth with seasonal-varying discharge (Fekete et al., 2002). Besides, the unresolved vertical mixing is parameterized using the K-Profile scheme of Large et al. (1994). The bottom topography is derived from ETOPO2 (Smith and Sandwell, 1997).

The adjoint method brings the model simulation close to available observations by iteratively adjusting control variables to minimize a quadric target function *J* (cost function hereafter):

$$J(C_{ini}, C_{atm}(t)) = \sum_{t=1}^{T1}[y(t) - E(t)x(t)]^T R^{-2}[y(t) - E(t)x(t)] + C_{ini}^T P^{-2} C_{ini} + \sum_{t=0}^{T1} C_{atm}(t)^T Q_a^{-2} C_{atm}(t) \quad (1).$$

https://doi.org/10.5194/egusphere-2022-1099
Preprint. Discussion started: 18 October 2022

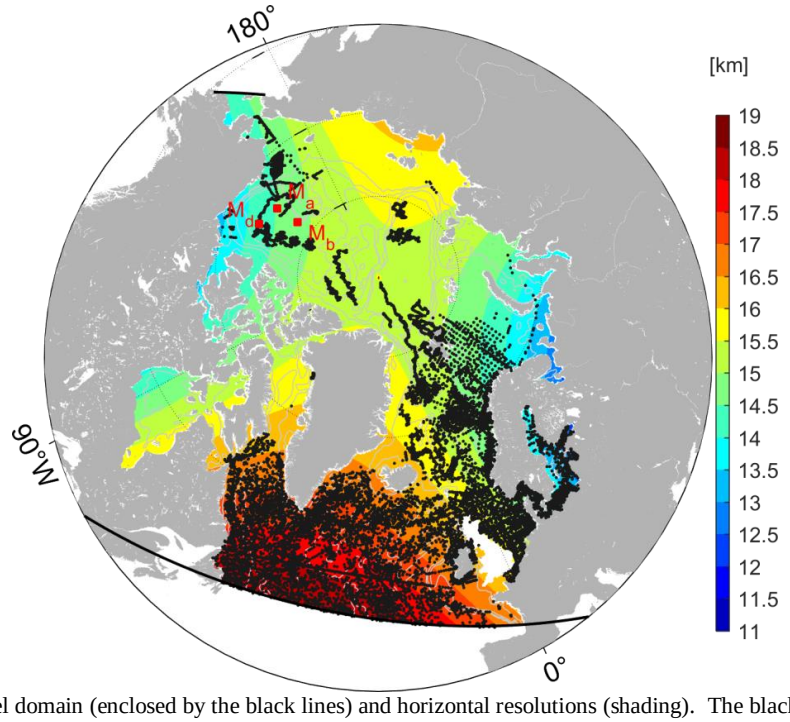

Figure 1. Model domain (enclosed by the black lines) and horizontal resolutions (shading). The black dots represent profile observations from EN4 datasets (Good et al., 2013), and the red rectangles show the three moorings from the Beaufort Gyre Exploration Project (BGEP).

With an assimilation window of one year (2012), the control variables consist of the initial condition (C_{ini}), including temperature, salinity, ice effective thickness, sea ice concentration, and daily atmosphere state on the model grid ($C_{atm}(t)$), which includes 10-m wind vectors, 2-m air temperature, 2-m specific humanity, precipitation, downwelling longwave, and net shortwave radiation. Overall, a total number of ~2.7×10^8 variables are adjusted.

On the right hand of Equation (1), the first term measures the model-data misfits weighted by the inverse error covariance matrices (R^{-2}). The following section will introduce the available measurements and their uncertainties (R). $y(t)$ and $x(t)$ are observations and the model state at time t, repectively. $E(t)$ maps the model state $x(t)$ to the corresponding observations $y(t)$. The last two terms are background terms of the initial condition (C_{ini}) and the time-varying atmospheric forcing ($C_{atm}(t)$) weighted by their inverse error covariance matrices (P^{-2} and Q^{-2}, respectively), which penalize their adjustments and provide complete information on the controls. Following Lyu et al. (2021b), prior uncertainties of the time-varying atmosphere state (Q_a) depend on geographic locations. They are computed as the variance of the nonseasonal variability of the corresponding variables using the NCEP-RA1.

During the optimization process, the adjoint of the coupled ocean-ice model is used to compute the gradients of the cost function J to the control variables, and a quasi-Newton algorithm (Gilbert and Lemaréchal, 2006) is used to reduce the cost function J iteratively. The optimization process continues until the cost function cannot be further reduced.

https://doi.org/10.5194/egusphere-2022-1099
Preprint. Discussion started: 18 October 2022

2.2 Observations and Prior Uncertainties

Both satellite and in-situ measurements (Table 1) are used to constrain the model simulations. In addition, sea ice draft measurements by up-looking sonar from the Beaufort Gyre Exploration Project (see Figure 1 for the locations) are used to validate the assimilation results independently.

Prior uncertainties follow our previous Arctic-focused synthesis study (Lyu et al., 2021b). Uncertainties of temperature and salinity depend on the depth and are set to 0.6° C and 0.3 PSU at the surface and 0.02° C and 0.02 PSU in the deep ocean; SIC uncertainties consist of representation errors (15% within 50 km from the coastlines and 10% over the open water) and instrument errors. Because of higher errors in low SIC and lower errors over open water, we modify the representation uncertainties by multiplicative factors of 0.85, 1.20, 1.10, and 1.00 for the observed SIC ranges of 0.00, <15%, 15%–25%, and 0.25%, respectively.

SIT errors are provided by the datasets and interpolated to our model grid. SLA uncertainties are set to 3.0 cm. Sea ice drift uncertainties are dominated by representation errors and are set to 0.04 m/s. In addition, we reduce the weight of the temperature and salinity climatology (WOA18) cost component by a factor of 20 and 10 to avoid overfitting to the climatology.

Table 1. Assimilated measurements.

Date sets	Resolution	Source
sea level anomaly	7 km	Copernicus Marine Environment Monitoring Service, http://marine.copernicus.eu
Sea surface temperature	25km	Remote Sensing System, http://www.remss.com/measurements/sea-surface-temperature/
T&S profiles	–	Good et al. (2013), https://www.metoffice.gov.uk/hadobs/en4/
Sea ice concentration	25km	Kaleschke et al. (2001) and Spreen et al. (2008), SSMI(2011-2012), http://icdc.cen.uni-hamburg.de/1/daten/cryosphere.html
Sea ice thickness	25km	(Ricker et al., 2017), https://spaces.awi.de/pages/viewpage.action?pageId=291898639
Sea ice drift	62.5km	(Lavergne et al., 2019), https://osi-saf.eumetsat.int/products/osi-405-c
WOA18	1°	Zweng et al. (2018), https://www.nodc.noaa.gov/OC5/woa18/woa18data.html

2.3 Viscos-Plastic Sea Ice Dynamics and Its Adjoint

In the coupled ocean-sea ice model, the following equation governs ice motions:

$$\mathrm{m}\frac{d\vec{u}}{dt} = -mf\vec{k} \times \vec{u} + \tau_{air} + \tau_{ocn} - \nabla\emptyset(0) + \nabla \cdot \sigma \quad (2)$$

where m is ice mass and $\vec{u}$ is ice motion vectors; τ_{air} and τ_{ocn} are the wind and ocean drags; $-\nabla\emptyset(0)$ is the tilt of the sea surface; and $\nabla \cdot \sigma$ is the divergence of the ice stress tensor σ_{ij} (i=1,2), representing the internal forces of sea ice.

In the viscous-plastic rheology of Hibler (1979), the stress tensor σ_{ij} is related to ice strain rate (ϵ_{ij}) and strength (P):

$$\sigma_{ij} = 2\eta(\epsilon_{ij}, P)\epsilon_{ij} + \left[\zeta(\epsilon_{i,j}, P) - \eta(\epsilon_{i,j}, P)\right]\epsilon_{i,j}\delta_{ij} - \frac{P}{2}\delta_{ij} \quad (3)$$

where δ_{ij} is the Kronecker delta ($\delta_{ij} = 1$ if i=j, otherwise 0). η and ζ are the bulk and shear viscosities, expressed as:

https://doi.org/10.5194/egusphere-2022-1099
Preprint. Discussion started: 18 October 2022

$$\zeta = \frac{P}{2\Delta_{reg}} \quad (4)$$

$$\eta = \frac{P}{2e^2\Delta_{reg}} \quad (5)$$

where

$$\Delta = [(\epsilon_{11}^2 + \epsilon_{22}^2)(1 + e^{-2}) + 2(1 - e^{-2})\epsilon_{11}\epsilon_{22} + 4e^{-2}\epsilon_{12}^2]^{\frac{1}{2}} \quad (6)$$

e is the ratio of normal stress to shear stress and is set to 2.0; $\Delta_{reg} = \max(\Delta, \Delta_{min})$ with Δ_{min} equals 1.0×10^{-10}. Sea ice strain rate is computed as:

$$\epsilon_{ij} = \frac{1}{2}\left(\frac{\partial u_i}{\partial x_j} + \frac{\partial u_j}{\partial x_i}\right) \quad (7).$$

The ice strength P depends on sea ice effective thickness (H) and concentration (C):

$$P = P^* H \cdot \exp(-C^* \cdot (1 - C)) \quad (8)$$

P^* and C^* are the ice compressive strength constant and ice strength decay constant and are set to 2.75×10^4 N m^{-2} and -20.0.

The dependence of the internal force term ($\nabla \cdot \sigma$) on ice velocity is strongly nonlinear, leading to an unstable adjoint of the coupled ocean-sea ice system. Therefore, previous studies (Koldunov et al., 2017; Lyu et al., 2021b) used an adjoint of a free drift sea ice model (without adjoint of $\nabla \cdot \sigma$). Toyoda et al. (2019) pointed out that the full adjoint of Equation (2) can be stabilized by eliminating the dependence of bulk and shear viscosities on strain rate (ϵ_{ij}).

Following the study of Toyoda et al. (2019), we eliminate the dependence of bulk and shear viscosities on ϵ_{ij} in the adjoint of Equation (2). Besides, we note that there are still strong sensitivities which hamper the convergence of optimization. We set the adjoint sensitivities of ice velocity to zero if the local sensitivity is 50 times larger than the global mean of their absolute values. The other modifications on the adjoint model are the same as in Lyu et al. (2021b).

Based on the adjoint of a free-drift sea ice model (adjoint-FD hereafter) and the viscous-plastic sea ice dynamics (adjoint-VP hereafter), we compute over the period January 1 to 31 January 31, 2012 sensitivities of domain-integrated sea ice volume with respect to the atmospheric forcings and the initial conditions. Similar to Toyoda et al. (2019), adjoint-FD shows much stronger sensitivities to wind than adjoint-VP (Figure 2a, b) in the central Arctic Ocean. Along the SIEs of the Atlantic sectors, adjoint-VP reveals that the towards-ice wind anomalies increase total sea ice (Figure 2b) since they prevent ice from drifting to the warm Atlantic water. However, adjoint-FD shows strong sensitivities along the SIE of the Atlantic sectors, but both towards-ice and off-ice wind anomalies appear, potentially resulting in ice convergence.

Furthermore, we add daily wind perturbations, computed by scaling the adjoint sensitivities (Figure 2a, b) that the maximum perturbations are 1.0 m s^{-1}, to the 6-hourly wind from NCEP-RA1 and examine their impacts on sea ice changes. As expected, sea ice effective thickness (Figure 2c, d) changes are mainly along the SIEs in the Atlantic sectors, and wind perturbations from adjoint-FD lead to negative effective changes northeast of Greenland. In the central Arctic Ocean with compact ice, the internal forces $\nabla \cdot \sigma$.contradicts the impacts of wind perturbations. Therefore, despite the strong adjoint sensitivities to the wind in adjoint-FD, we note that the resulting wind

https://doi.org/10.5194/egusphere-2022-1099
Preprint. Discussion started: 18 October 2022

perturbations change effective thickness only slightly (Figure 2c), which is comparable to that in adjoint-VP (Figure 2d).

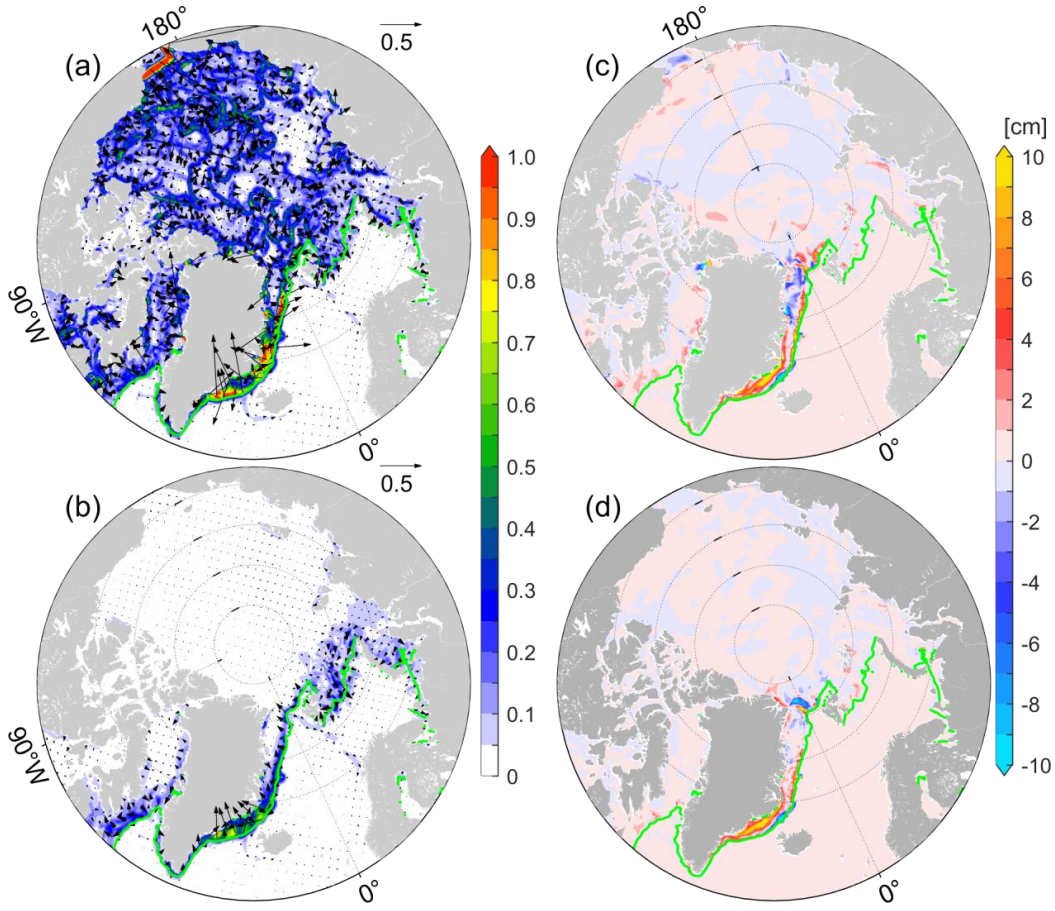

Figure 2. Sensitivities of total sea ice volume to wind vecors (in $0.1\times km^3$ $(m\ s^{-1})^{-1}$, shadings for amplitudes) using the adjoint of (a) a free-drift sea ice dynamic and (b) full viscous-plastic sea ice dynamics with modifications in section 2.3. Panels (c)-(d) are the mean effective thickness changes by perturbing the wind with the corresponding adjoint sensitivities multiplied by a factor of 10^{-8}. The green lines are the SIE in January 2012.

Besides overestimating the sensitivities to wind, adjoint-FD may also degrade the usefulness of the adjoint sensitivities in optimization. Therefore, we perform two assimilation experiments to comprehensively evaluate the impacts of including the adjoint of sea ice rheology on ocean and sea ice estimation.

3 Model-Data Misfits Reductions and Residuals

3.1 Evaluation of the Optimization

In adjoint-FD and adjoint-VP, 13 and 32 iterations were performed before the cost function could not be further reduced, resulting in an overall cost reduction of 32.3% and 40.2% (see Table 2 for details), respectively. Of the individual cost constituents, satellite-observed SST and SIC contribute to ~25.3% and 39.7% of the total cost, which

https://doi.org/10.5194/egusphere-2022-1099
Preprint. Discussion started: 18 October 2022

are reduced significantly after optimization. The cost of temperature ($J_{profile\_T}$) and salinity ($J_{profile\_S}$) profiles are also considerably reduced, especially in the adjoint-VP experiment. The rest of the cost constituents are also brought down slightly. Overall, including the adjoint of sea ice rheology further reduces the total cost by 7.9% and individual cost constituents, especially J_{sst}, $J_{profile\_T}$ and $J_{profile\_S}$. Based on iterations 0, 13 in adjoint-FD, and 32 in adjoint-VP of the optimization, we will focus on the sea ice state and ocean temperature to evaluate the impacts of using the adjoint of full sea ice dynamics.

Table 2. Normalized costs and reductions in the two optimization runs.

Cost constituent	**Control run**	**Adjoint-FD**		**Adjoint_VP**	
	Normalized cost (%)	Normalized cost (%)	Percentage reduction (%)	Normalized cost (%)	Percentage reduction (%)
J_{Total}	100	67.7	32.3	59.8	40.2
J_{SLA}	2.2	2.1	4.6	2.1	4.6
J_{SST}	25.3	15.4	39.1	12.9	49.0
$J_{profile\_T}$	6.9	6.5	5.8	4.3	37.7
$J_{profile\_S}$	5.8	5.9	-1.7	4.5	22.4
J_{SIC}	39.7	18.4	53.7	18.1	54.4
J_{SIT}	3.6	3.1	13.9	2.7	25.0
J_{SID}	4.5	4.4	2.2	4.3	4.4
J_{WOA_T}	6.6	6.6	0.0	6.2	6.1
J_{WOA_S}	5.4	5.3	1.9	4.7	13.0

3.2 Sea Ice State

3.2.1 Residual Errors of SIC and SIT

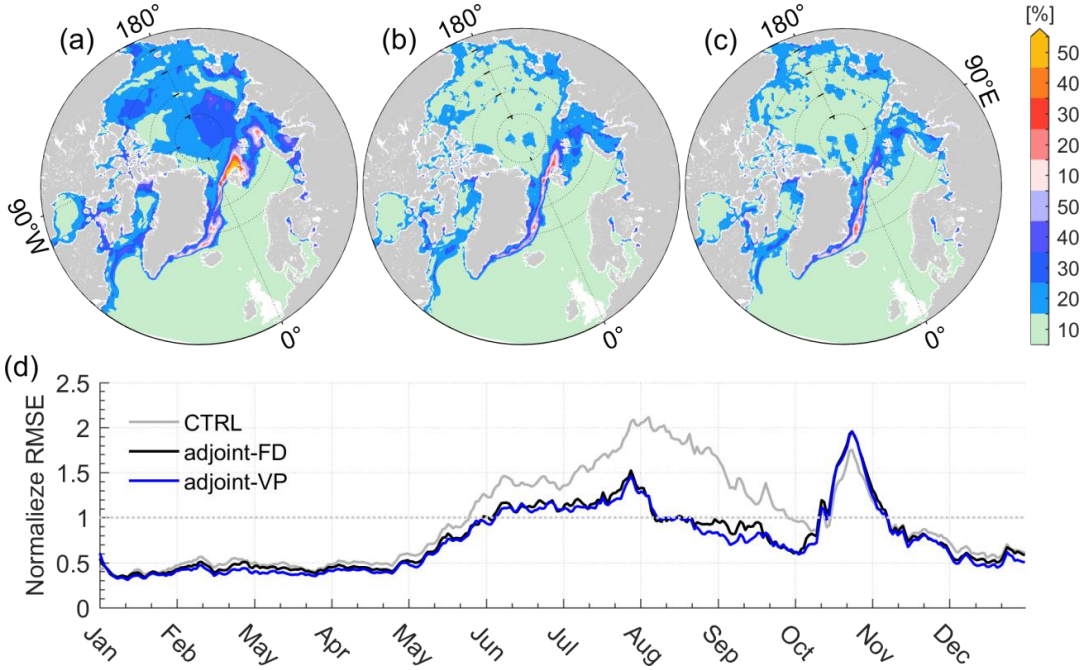

https://doi.org/10.5194/egusphere-2022-1099
Preprint. Discussion started: 18 October 2022

Figure 3. Root mean square errors (RMSEs) of SIC between the satellite measurements and (a) the control run, (b) adjoint-FD, and (c) adjoint-VP, respectively. Panel (d) shows the temporal variations of RMSEs in the three simulations.

Satellite visual, infrared, and microwave technologies have been applied to monitor SIC with high frequencies and quality, which is of high priority in the global and Arctic-focused synthesis (Chevallier et al., 2017; Uotila et al., 2019). Previous studies (Fenty and Heimbach, 2013; Lyu et al., 2021a; Lyu et al., 2021b) indicated that SIC could be improved significantly by adjusting the atmospheric forcings slightly. Here, we explore the residual errors in the optimization runs.

The root mean square errors (RMSEs) of SIC averaged over 2012 (Figure 3a-c) and normalized by the prior errors and averaged over the model domain (Figure 3d) show the geographical distribution and temporal evolution of SIC errors, respectively. The normalized RMSEs should be close to 1.0 if the optimization found a model simulation consistent with the observations and the prior uncertainties.

The control run (Figure 3a) shows pronounced RMSEs in the Beaufort Gyre (~15%), the central Eurasian Basin (15%~20%), the marginal seas (15%~20%), and sea ice extent regions of the Atlantic sector (30%-50%). The normalized RMSEs reveal that SIC errors remain small (~0.5) and grow quickly from May-September when the sea ice melts (Figure 3d). Normalized RMSEs up to 1.5 are observed in October, but quickly drop in November (Figure 3d).

Both assimilation experiments reduce the SIC errors to less than 5% in the central Arctic Ocean and 10% in the marginal seas. SIC errors up to 20% exist in the Atlantic sector, where sea-ice shows strong nonlinearity and the tangent linear model could only capture part of the sea-ice changes (Appendix B in Lyu et al., 2021a). Normalized SIC errors from May to September have also been reduced close to 1.0 by assimilation of the daily SIC observations (Figure 3d). However, SIC errors in October remain significant (Figure 3d) since the observed sea ice recovered much faster than in the three simulations (not shown here). This delayed sea ice recovery in the model may related to model uncertain parameters, such as demarcation thickness between thin and thick ice which decides the initial sea ice thickness formed in open water.

The control run shows sea ice thickness errors up to 1.0 m in regions north and south of the Fram Strait and around 0.4~0.7 m in the Beaufort Gyre. In the Beaufort Gyre, the SIT errors are reduced to less than 0.3 m in adjoint-VP (Figure 4c) and around 0.3-0.5 m in adjoint-FD (Figure 4b). Similar to SIC errors, SIT errors up to 1.0 m remain along the East Greenland Current, which seems to increase in the two assimilation experiments. The temporal evolutions of normalized RMSEs show that SIT errors grow quickly from February to April (Figure 4d). Both assimilation experiments bring down the SIT errors, especially in adjoint-VP from January to April (Figure 4d). However, the normalized RMSEs of SIT averaged over the model domain remain smaller than 1.0 and seem to grow larger during the melting season, indicating that the prescribed constant error is not entirely appropriate. More accurate SIT observations (e.g., halve the uncertainties) and SIT observations during the melting season are required to facilitate a significant impact on the solution.

https://doi.org/10.5194/egusphere-2022-1099
Preprint. Discussion started: 18 October 2022

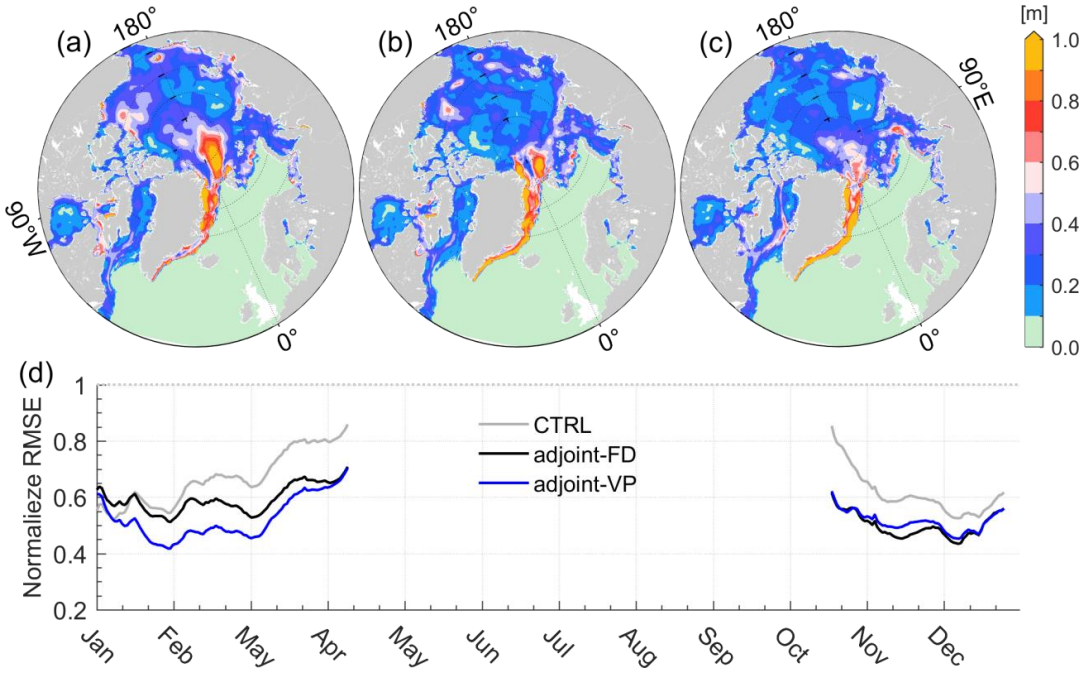

Figure 4. Root mean square errors (RMSEs) of SIT between the satellite measurements and (a) the control run, (b) adjoint-FD, and (c) adjoint-VP. Panel (d) shows the temporal variations of RMSEs in the three simulations.

3.2.2 The BGEP Mooring Measurements

Independent sea ice draft measured by up-looking-sonar (ULS) from BGEP moorings (M_a, M_b, and M_d in Figure 1) is used to validate the simulated sea-ice draft. The simulated snow depth (d_{snow}) and SIT (d_{SIT}) are used to compute the sea ice draft following Tilling et al. (2018):

$$\text{draft} = \frac{\rho_i \times d_{SIT} + \rho_s \times d_{snow}}{\rho_w} \quad (9)$$

where ρ_i, ρ_s, ρ_w are the density of sea-ice, snow, and water and are set to 910.0, 330.0, and 1027.5 kg m^{-3} as in our model.

https://doi.org/10.5194/egusphere-2022-1099
Preprint. Discussion started: 18 October 2022

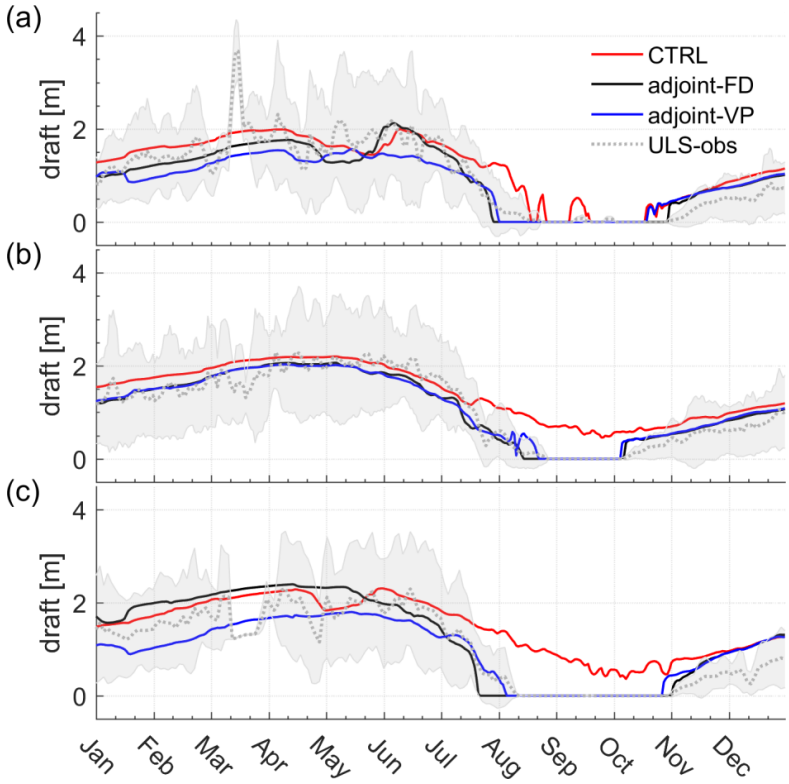

Figure 5. Daily time series of sea ice draft (grey lines) and the daily standard deviation (shadings) at the mooring locations (a) M_a, (b), M_b, and (c) M_d compared with the three model runs (see the legends). ULS-observed sea ice draft is smoothed with 5-days running average.

3.3 Ocean Temperature

Ocean temperature changes are closely related to sea ice changes. Adjoint-VP introduces more pronounced ocean temperature changes than adjoint-FD. Here, we explore ocean temperature changes after assimilation.

Temperature profiles in the Arctic Ocean are much less than in the North Atlantic Ocean (black dots in Figure 1). In the Arctic Ocean, adjoint-FD only reduces temperature errors over the top 20 m, while adjoint-VP reduces temperature errors up to 0.4 ° C over the top 1000 m (Figure 6a). In the North Atlantic Ocean, adjoint-VP results in more pronounced RMSEs reduction up to 0.3 ° C than adjoint-FD (Figure 6b).

https://doi.org/10.5194/egusphere-2022-1099
Preprint. Discussion started: 18 October 2022

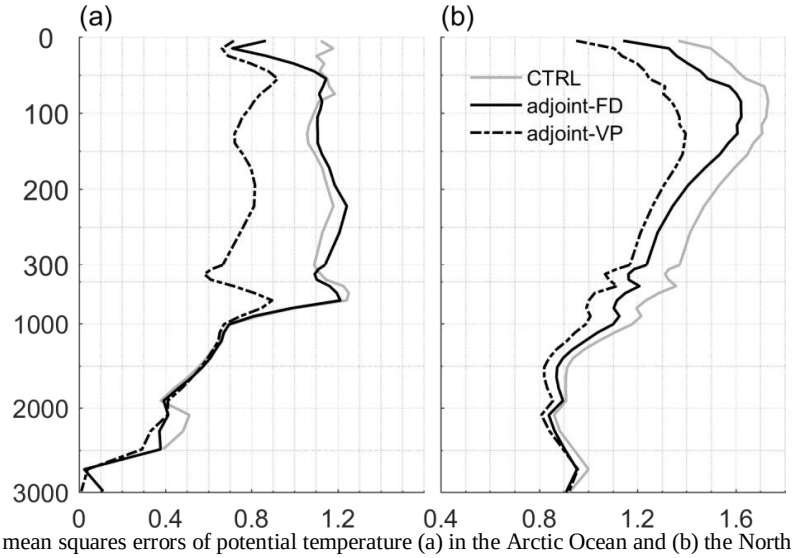

Figure 6. Root mean squares errors of potential temperature (a) in the Arctic Ocean and (b) the North Atlantic Ocean in the three runs.

Relative temperature error reductions over the top 50 m reveal an overall improvement of temperature with occasional degradations (Figure 7a, b). Adjoint-VP results in a more significant error reduction than adjoint-FD in the North Atlantic Ocean (Figure 7a, b). In the southern Beaufort Gyre, the Laptev and Kara seas, and north of Svalbard, both adjoint-VP and adjoint-FD increase the ocean temperature (over 50 m) since the two optimization runs reproduce the early retreat of sea ice well, allowing more solar heating of the open water. In the North Atlantic Ocean, adjoint-VP achieves more considerable temperature changes than adjoint-FD both over the top 50m (Figure 7c, d) and from 50m-700m (Figure 7e, f). In the Arctic Ocean, In the layer of 50-700 m, adjoint-VP further introduced negative temperature corrections between 50-700 m (Figure 7f), especially near the profiles locations (see dots in Figure 7b), resulting from more iterations performed.

https://doi.org/10.5194/egusphere-2022-1099
Preprint. Discussion started: 18 October 2022

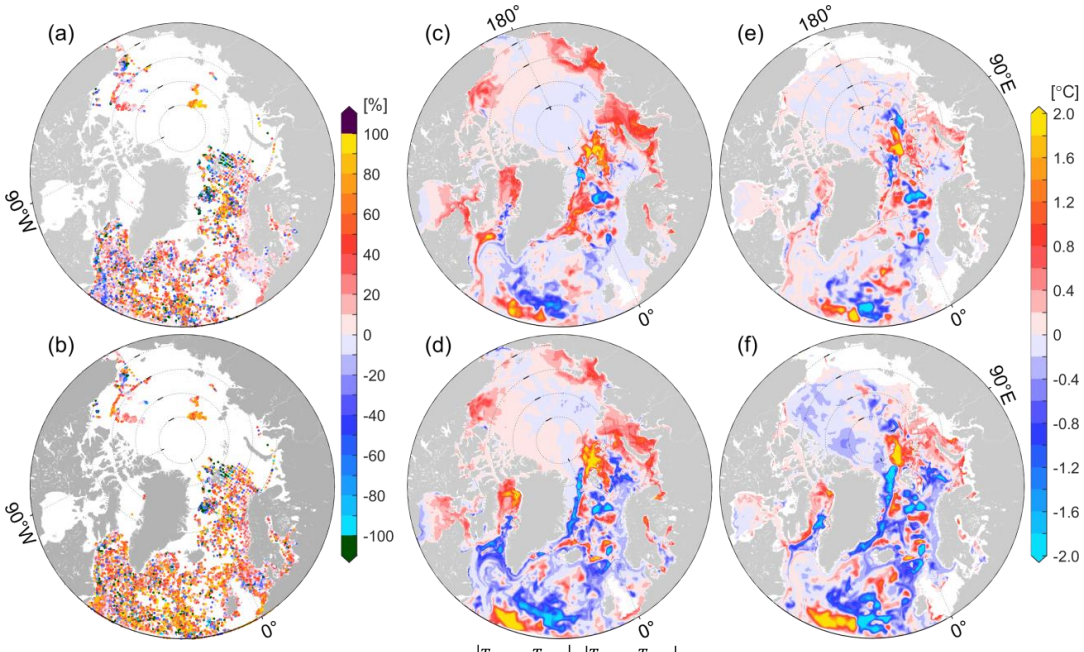

Figure 7. Relative temperature error reduction ($-\frac{|T_{opti}-T_{obs}|-|T_{ctrl}-T_{obs}|}{|T_{ctrl}-T_{obs}|}\times 100\%$) over the top 50 m at the profile locations in (a) adjoint-FD and (b) adjoint-VP. Values >100% means over-adjustment. Panels (c) and (d) are temperature differences of adjoint-FD and adjoint-VP to the control run averaged over the top 50m, respectively. Panels (e) and (f) are the same as Panels (c) and (d), but for layers 50-700m.

In summary, adjoint-FD and adjoint-VP reproduce the SIC variations well in the Arctic Ocean, which further reduces ocean temperature errors over the top layer by improving atmosphere-ocean heat flux. adjoint-VP achieves more significant corrections to the ocean temperature over the open water and in the intermediate layer of the Arctic Ocean than adjoint-FD.

4 Adjustments of the Control Variables

The adjoint models project the model-data misfits onto the gradient of the objective function with respect to all control variables simultaneously, which is used by the optimization algorithim to adjust the control variables. In this section, we compare adjustments of the control variables in the adjoint-FD and adjoint-VP, and evaluate contributions of individual adjustments of the control variables on the cost function reduction.

Among all the control variables, wind vectors and 2-m air temperature are adjusted considerably in adjoint-FD and adjoint-VP, which also show significant differences. Besides, adjoint-VP induce more prounced adjustments of initital temperature and salinity than adjoint-FD (not shown here).

https://doi.org/10.5194/egusphere-2022-1099
Preprint. Discussion started: 18 October 2022

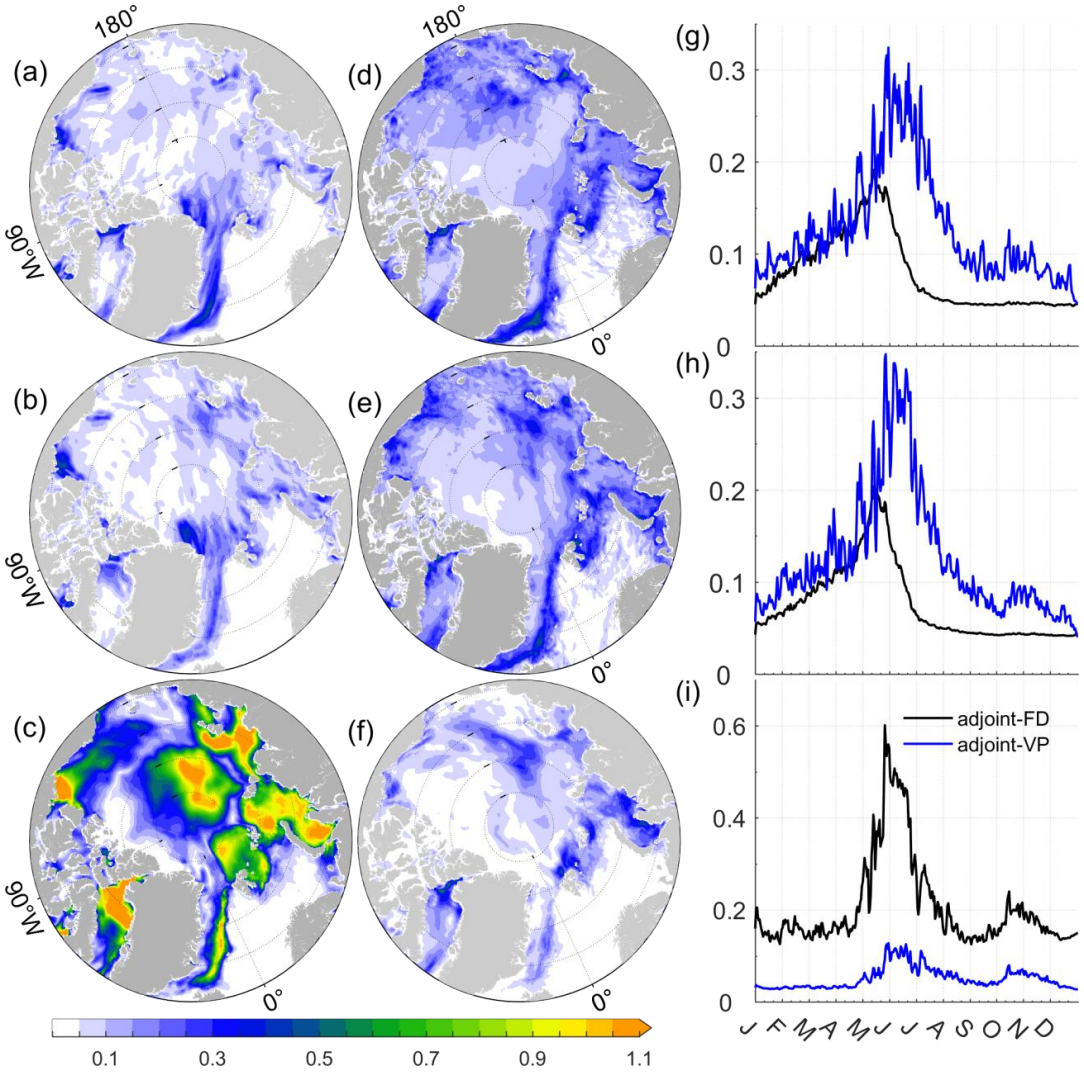

Figure 8. Adjustments of (a) wind *u*-component, (b) wind v-component, and (c) 2 meter air temperature normalized by their prior uncertainties in adjoint-FD and averaged over 2012. Panels (d)-(f) are similar to (a)-(c) but for adjoint-VP. Panels (g)-(i) are area average of the adjustments of the wind *u*-component, wind v-component, and 2-m air temperature normalized by their prior uncertainties in adjoint-FD and adjoint-VP.

Moderate wind vector adjustments (with normalized adjustments of 0.2~0.3) occur over the seasonal ice-covered regions (Figure 8a, b, d, and e) with more prounced adjustments in adjoint-VP (Figure 8d, e) than adjoint-FD (Figure 8a, b). Besides, maximum adjustments of wind vectors appear in June in adjoint-VP but in May in adjoint-FD (Figure 8g). adjoint-FD adjusts 2-m air temperature more significantly than adjoint-VP in the Arctic Ocean (Figure 8c, f) and throughout 2012 (Figure 8i).

In adjoint-FD, the 2-m air temperature adjustments normalized by their prior uncertainties exceed 1.0 over the seasonal sea ice-covered regions and the central Arctic Ocean (Figure 8c). While adjoint-VP adjust 2-m air

https://doi.org/10.5194/egusphere-2022-1099
Preprint. Discussion started: 18 October 2022

temperature moderately with normalized adjustments of ~0.2-0.3 over the seasonal sea ice-covered regions. The maximum adjustments occur in June in the two optimization runs (Figure 8i).

Table 3. Contributions of adjustments of 2-m air temperature, wind vectors, initial temperature and salinity (Initial T &S), and the remaining control variables (including initial sea ice effective thickness and concentration, 2-m specific humanity, precipitation, downwelling longwave, and net shortwave radiation) on the total cost reduction, SIC, SST, and temperature profiles in the two optimization runs.

	Adjoint-FD (%)				**Adjoint-VP (%)**			
	2-m air temperature	Wind vectors	Initial T & S	The rest	2-m air temperature	wind	Initial T & S	The rest
J_{total}	29.0	17.5	6.0	3.0	5.3	52.6	25.1	5.0
J_{SIC}	25.5	19.8	2.4	1.2	4.5	64.9	10.1	2.4
J_{SST}	41.0	8.6	10.1	5.5	8.4	47.4	29.6	6.4
J_{prof_T}	3.9	4.9	4.3	4.3	4.4	40.9	182.0	7.9

By replacing the adjusted initial temperature and salinity, wind vectors, 2-m air temperature, and the remaining control varables (including initial sea ice effective thickness and concentration, 2-m specific humanity, precipitation, downwelling longwave, and net shortwave radiation) with their original values and estimate their controbutions to the total cost reductions and individual components, including SIC, SST, and temperature profiles (see Table 3).

The small contributions of adjustments of the remaining control variables ("The rest" in Table 3) variables to the cost function reductions in adjoint-FD and adjoint-VP highlight the importance of adjustments on the initial temperature and salinity, wind vectors and 2-m air temperature simultaneously. In adjoint-FD, adjustments of 2-m air temperature and wind vectors dominate the cost function reduction, especially SIC components. In contrast, adjoint-VP rely more on adjustments of wind vectors and initial temperature and salinity. Besides, the more prounced water temperature improvements (see Figure 7) in adjoint-VP are mostly attributed to adjustments of initial temperature and salinity (Table 3).

Overall, adjoint-FD improves the model simulation through adjusting 2-m air temperature strongly and wind vectors moderately. Adjoint-VP adjusts initial conditions, 2-m air temperature, and wind vectors moderately while achieving a much larger reduction of the model-data misfits. This leads to the conclusion that the large 2-m air temperature adjustments in adjoint-FD are likely an overcompensation for wind errors that could not be corrected appropriately because of large errors in the respective cost function gradients.

5 The Impacts On Sea Ice Retreat Processes

A unique characteristic of the adjoint-based synthesis is that its physical processes are described by the governing equations of the model, allowing us to quantify the sea ice loss and the contributions of ice dynamics and sea ice-ocean-atmosphere fluxes through a closed budget analysis. Since the two optimization runs reproduce the retreat of sea ice cover well, we further explore sea-ice effective thickness changes based on the model governing equations:

$$H_{Sep} = H_{Apr} + \int(-\nabla\cdot(\vec{u}\mathrm{h}) + F_{oi} + F_{ai} + F_{res})\,dt \quad (10).$$

Ice effective thickness on September 20 (H_{Sep}) depends on effective thickness on April 10 (H_{Apr}), ice advective flux ($-\nabla\cdot(\vec{u}\mathrm{h})$), ocean-sea ice heat flux (F_{oi}) depending on ocean temperature difference to freezing temperature (Maykut and Mcphee, 1995), atmosphere-sea ice flux (F_{ai}) consisting of radiation and turbulence fluxes, and a residual

https://doi.org/10.5194/egusphere-2022-1099
Preprint. Discussion started: 18 October 2022

term (F_{res}) including a snow flooding effect and a source term to correct negative effective thickness to zero. Since contributions of the residual terms are small, we will not show them in the analysis below.

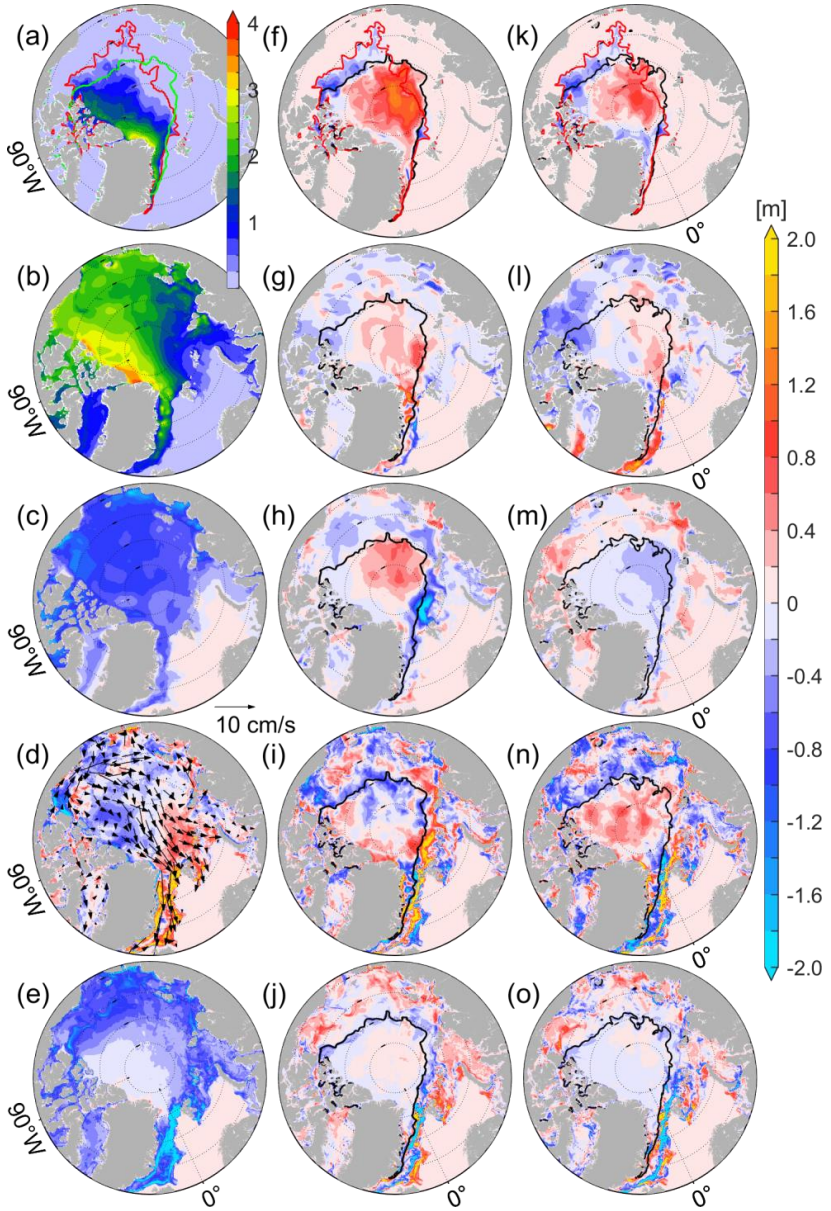

Figure 9. Sea ice effective thickness on (a) September 20 and (b) April 10, and ice changes due to (c) F_{ai}, (d) F_{adv}, and (e) F_{oi}. Panels (f)-(j) and (k)-(o) are differences in the corresponding terms to the control run for (f-j) adjoint-FD and (k)-(o) adjoint-VP, respectively. The green and red lines are the September SIEs from satellite measurement and the three runs, respectively.

https://doi.org/10.5194/egusphere-2022-1099
Preprint. Discussion started: 18 October 2022

In the control run, the September sea ice covers more area than satellite observations in the Pacific sectors and less area in the eastern Eurasian Basin (red and green lines in Figure 9a). On April 10, effective thickness is up to 1.5 m in the Eurasian Basin and ~2.0-2.5m in the Pacific sectors (Figure 9b). From April 10 to September 20, atmosphere-sea ice heat flux melts the ice from the top, which is more pronounced in the Pacific sectors (-1.0~-2.0 m) than in the Eurasian Basin and the central Arctic Ocean (-0.6 m, Figure 9c). F_{adv} moves ice from the central Arctic Ocean to the western Eurasian Basin and out through the Fram Strait (Figure 9d), which is then melted by the warm Atlantic water (Figure 9e). Besides, ocean-sea ice heat flux melts sea ice up to -1.2 m over the seasonal sea ice-covered areas (Figure 9e).

Adjoint-FD and adjoint-VP reproduce the observed September SIE very well (black lines in Figure 9f, k). The two optimization runs remove the extra sea ice the Pacific sectors of the control run in comparison to the satellite observations (areas enclosed by the red and black lines in Figure 9f, k) through F_{adv} (Figure 9i, n). At the same time, in the central Arctic Ocean, adjoint-FD and adjoint-VP thicken the sea ice up to 1.2 and 0.8 m (Figure 9f, k), respectively.

On April 10, adjoint-FD/adjoint-VP show thiner sea ice by -0.2/-0.6 m in the southern Beaufort Gyre and the marginal seas (Figure 9g, l) and thicker sea ice in the Eurasian Basin and the central Arctic Ocean by 0.4 m. During the melting season, adjoint-FD and adjoint-VP show differences mainly in F_{ai} (Figure 9h, m)and F_{adv} (Figure 9i, n). In adjoint-FD, F_{ai} melts more ice in the seasonal sea ice-covered regions (-0.4~-2.0 m) and less ice in the central Arctic Ocean up to 0.6 m (Figure 9h), contributing to the increased effective thickness in September in the central Arctic Ocean. In adjoint-VP, the thickened September ice thickness in the central Arctic Ocean is mainly induced by F_{adv} through ice convergence (Figure 9n). Both adjoint-FD and adjoint-VP enhance ice loss in the marginal seas and the southern Beaufort Gyre (Figure 9j, o) with similar patterns and amplitudes, reflecting that basal melting is mainly related to the SIC changes through ice-albedo feedbacks.

We note that a much stronger sea ice loss process occurs from May 10 to June 10 in adjoint-FD than in adjoint-VP, mainly related to surface melting anomalies. During this period, the Arctic Ocean observations rely most on SIC measurements. Both the two optimization run reproduce the observed SIEs well (green and red lines in Figure 10a, d, and b, e), with adjoint-VP (Figure 10b) slightly betterthan adjoint-FD in the Barent and Kara Seas on June 10 (Figure 10e).

On May 10, sea ice has been thinned to ~1.0 m between the central Arctic Ocean and the Chukchi Sea (Figure 10a). adjoint-VP shows thinner ice up to -0.6 m than adjoint-FD in the southern Beaufort Gyre, north of Svalbard and Franz-Josef-Land (Figure 10d).

From May 10 to June 10, sea ice is melted in the southeastern Beaufort Gyre, the Laptev Sea, the Kara Sea, and north of Svalbard and Franz-Josef-Land, creating open water and polynya (Figure 10b, e), with adjoint-FD (Figure 10b) shows much stronger melting than adjoint-VP (Figure 10e). In the Kara and Barents Seas, the intense ice melt in adjoint-FD leads to a further retreat of SIEs (red line in Figure 10b) compared with observations and adjoint-VP (red line in Figure 10e) by June 10.

In adjoint-FD, surface melting contributes to strong sea ice thinning up to 0.8-2.0 m (shading in Figure 10c), mainly caused by 2-m air temperature adjustments (contours in Figure 10c). As shown, 2-m air temperature is

https://doi.org/10.5194/egusphere-2022-1099
Preprint. Discussion started: 18 October 2022

386 increased by more than 8° C in the marginal seas (prior air temperature uncertainties are ~2-5° C) to facilitate the
387 intense surface melting. In the central Arctic Ocean, negative 2-m air temperature adjustments up to -6° C result in
388 little ice melt. In contrast, adjoint-VP shows surface melting of -0.4 m with reasonable air temperature adjustments
389 (<2° C, Figure 10f).

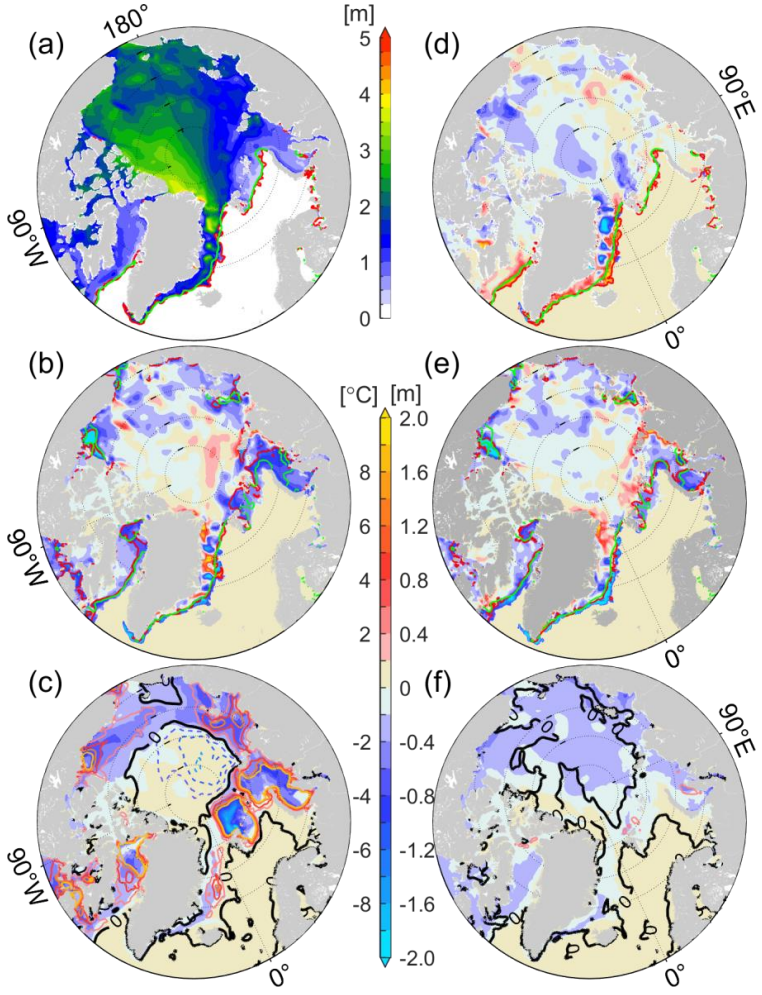

390

391 Figure 10. (a) Sea ice effective thickness on May 10 in adjoint-FD. Panels (b) and (c) are the sea ice effective thickness
392 changes and contributions from atmosphere-sea ice heat flux $\int F_{ai}$ from May 10 to June 10. Panel (d) is sea ice
393 effective thickness differences between adjoint-VP and adjoint-FD (adjoint-VP minus adjoint-FD) on May 10. Panels
394 (e)-(f) are similar to Panels (b)-(c) but for adjoint-VP. The red and green lines indicate the model-simulated (a-b for
395 adjoint-FD; d-e for adjoint-VP) and satellite-observed sea ice extent on (a, d) May 10 and (b, e) June 10. The contours
396 in panels (c) and (f) show the adjustments of 2-m air temperature (see the legend for the amplitude).

397 Overall, the two optimization runs successfully reproduce the sea ice retreat process in 2012 by assimilating
398 satellite and in-situ measurements. However, the sea ice retreat processes differ in the two optimized solutions,
399 especially from May to June, when Arctic Ocean observations rely mostly on satellite-measured SIC. Considering the

https://doi.org/10.5194/egusphere-2022-1099
Preprint. Discussion started: 18 October 2022

amplitude of air temperature adjustments, the adjustments of the control variables in adjoint-VP are more reasonable than adjoint-FD, and adjoint-VP seems to project model-data misfits to the control variables more reasonably than adjoint-FD.

6 Conclusions

The adjoint model is a powerful way to calculate sensitivities of a target function to model variables and has been applied to the coupled Arctic ocean and sea ice models for sensitivity studies (Heimbach et al., 2010; Kauker et al., 2009; Koldunov et al., 2013) and state estimate (Fenty and Heimbach, 2013; Koldunov et al., 2017; Lyu et al., 2021b; Nguyen et al., 2021). However, due to the persistent instability issues, traditionally the adjoint of sea ice dynamics was excluded or simplified to the adjoint of a free-drift sea ice model, which potentially hampers the accuracy of the coupled ocean and sea ice estimation.

Based on the study of Toyoda et al. (2019) and the coupled ocean-sea ice modeling and adjoint assimilation system (Lyu et al., 2021a), we stabilize the adjoint of a viscous-plastic sea ice dynamic model and test the impacts of including the rheology on estimating the spatio-temporal variations of Arctic ocean and sea ice state.

Two optimizations with incuded and excluded rheology were performed and both show reduced SIC and SIT errors and both reproduce the sea ice retreat well. With the improved SIC retreat processes, adjoint-FD and adjoint-VP also show similar ocean temperature changes in the marginal seas and the southern Beaufort Gyre since solar radiation heats the open water quickly as the sea ice retreats. With the improved adjoint of sea ice dynamics, adjoint-VP allows much stronger adjustments of the initial temperature, resulting in a much more significant improvement in the temperature in the North Atlantic Ocean and the intermediate layer (50-700 m) of the Arctic Ocean.

Desipite that adjoint-FD compute much stronger sensitivities of the cost function to the wind vectors than adjoint-VP, we note that adjoint-FD adjusts more (less) on 2-m air temperature (wind vectors) than adjoint-VP. It seems that adjoint sensitivities of wind vectors in adjoint-FD is less efficient to reduce the cost function than adjoint-VP during the optimization. And adjoint-FD adjusts 2-m air temperature strongly to reduce the model-data misfits while adjoint-VP adjusts all the control variables considerably to improve the model simulation.

Using a sea ice budget analysis, we further examine the sea ice retreat processes in adjoint-FD and adjoint-VP. The control run simulates extra ice in the Pacific sector on 20. September, which is removed through ice advective flux in the optimization runs. At the same time, sea ice in the central Arctic Ocean is thickened compared with the control run caused by reduced surface melting in adjoint-FD and ice convergence in adjoint-VP. We note that adjoint-FD and adjoint-VP show different ice thinning processes from May 10 to June 10 and in the marginal seas. Adjoint-FD showed thicker ice in the marginal seas than adjoint-VP, which is melted by increasing the air temperature enormously (up to 8° C). In adjoint-VP, sea ice thinning is moderate with more reasonable adjustments of air temperature. Therefore, the improvement of the adjoint model in adjoint-VP maps the model-data misfits better to the control variables than adjoint-FD.

https://doi.org/10.5194/egusphere-2022-1099
Preprint. Discussion started: 18 October 2022

Parameter uncertainties significantly impact ocean and sea ice simulations (Lu et al., 2021; Massonnet et al., 2014; Sumata et al., 2019), and a lack of direct observations of key parameters potentially result in biases in the model simulation and predictions. The development of the adjoint of the viscous-plastic sea ice dynamics further introduces three parameters, including ice compressive strength constant (P^*), ice strength decay constant (C^*), and ration of normal stress to shear stress (e), into the adjoint model. Sensitivities of the model uncertain parameters could be calculated with the adjoint of the coupled ocean-sea ice model, providing chances to further improve ocean-sea ice estimates through jointly estimating state and parameters.

7 Data availability

The data used to create the plots in the paper are available at Pangaea (https://issues.pangaea.de/browse/PDI-33039). Assimilated observations are listed in Table 1; and the up-looking sonar observed sea ice draft are from the Beaufort Gyre Exploration Project (BGEP, https://www2.whoi.edu/site/beaufortgyre/).

Author contribution. G. Lyu designed the experiments, conducted the experiments and analysis. A. Koehl contributed to the experiment design and interpretations. G. Lyu wrote the first draft. A. Koehl, D. Stammer, X. Wu, and M. Zhou contributed to reviewing and editing the manuscript.

Competing interests. The authors declare that they have no conflict of interest.

Acknowledgments

This work was funded partly by the Open Fund Project of Key Laboratory of Marine Environmental Information Technology, Ministry of Natural Resources of the People's Republic of China to G. Lyu and by the Shanghai Frontiers Science Center of Polar Science (SCOPS) to M. Zhou. We thank NCEP for offering the NCEP/NCAR-RA1 reanalysis. Thanks to ICDC at University of Hamburg and Alfred Wegener Institute for supplying the ASI-SSM/I sea ice concentration and CryoSat-2/SMOS L4 datasets. We also acknowledge the Met Office, the Copernicus Marine Service, and the Beaufort Gyre Exploration Project for archiving and sharing the EN4, the along-track SLA , and sea ice draft datasets used in assimilation and independent validation.

References

AMAP, Arctic Climate Change Update 2021: Key Trends and Impacts. Summary for Policy-makers. Arctic Monitoring and Assessment Programme (AMAP), Tromsø, Norway. 16 pp, 2021.
Buckley, M. W., Ponte, R. M., Forget, G., and Heimbach, P.: Low-Frequency SST and Upper-Ocean Heat Content Variability in the North Atlantic, Journal of Climate, 27, 4996-5018, 10.1175/jcli-d-13-00316.1, 2014.
Chevallier, M., Smith, G. C., Dupont, F., Lemieux, J.-F., Forget, G., Fujii, Y., Hernandez, F., Msadek, R., Peterson, K. A., Storto, A., Toyoda, T., Valdivieso, M., Vernieres, G., Zuo, H., Balmaseda, M., Chang, Y.-S., Ferry, N., Garric, G., Haines, K., Keeley, S., Kovach, R. M., Kuragano, T., Masina, S., Tang, Y., Tsujino, H., and Wang, X.:

https://doi.org/10.5194/egusphere-2022-1099
Preprint. Discussion started: 18 October 2022

Intercomparison of the Arctic sea ice cover in global ocean–sea ice reanalyses from the ORA-IP project, Climate Dynamics, 49, 1107-1136, 10.1007/s00382-016-2985-y, 2017.
Comiso, J. C., Parkinson, C. L., Gersten, R., and Stock, L.: Accelerated decline in the Arctic sea ice cover, Geophysical Research Letters, 35, 10.1029/2007gl031972, 2008.
Fekete, B. M., Vörösmarty, C. J., and Grabs, W.: High-resolution fields of global runoff combining observed river discharge and simulated water balances, Global Biogeochemical Cycles, 16, 15-11-15-10, https://doi.org/10.1029/1999GB001254, 2002.
Fenty, I. and Heimbach, P.: Coupled Sea Ice–Ocean-State Estimation in the Labrador Sea and Baffin Bay, Journal of Physical Oceanography, 43, 884-904, 10.1175/jpo-d-12-065.1, 2013.
Forget, G., Campin, J. M., Heimbach, P., Hill, C. N., Ponte, R. M., and Wunsch, C.: ECCO version 4: an integrated framework for non-linear inverse modeling and global ocean state estimation, Geoscientific Model Development, 8, 3071, 2015.
Giering, R. and Kaminski, T.: Recipes for adjoint code construction, ACM Transactions on Mathematical Software (TOMS), 24, 437-474, 1998.
Gilbert, J. C. and Lemaréchal, C.: The module M1QN3, 2006.
Good, S. A., Martin, M. J., and Rayner, N. A.: EN4: Quality controlled ocean temperature and salinity profiles and monthly objective analyses with uncertainty estimates, Journal of Geophysical Research: Oceans, 118, 6704-6716, 10.1002/2013jc009067, 2013.
Heimbach, P., Menemenlis, D., Losch, M., Campin, J.-M., and Hill, C.: On the formulation of sea-ice models. Part 2: Lessons from multi-year adjoint sea-ice export sensitivities through the Canadian Arctic Archipelago, Ocean Modelling, 33, 145-158, https://doi.org/10.1016/j.ocemod.2010.02.002, 2010.
Heimbach, P., Fukumori, I., Hill, C. N., Ponte, R. M., Stammer, D., Wunsch, C., Campin, J.-M., Cornuelle, B., Fenty, I., Forget, G., Köhl, A., Mazloff, M., Menemenlis, D., Nguyen, A. T., Piecuch, C., Trossman, D., Verdy, A., Wang, O., and Zhang, H.: Putting It All Together: Adding Value to the Global Ocean and Climate Observing Systems With Complete Self-Consistent Ocean State and Parameter Estimates, Frontiers in Marine Science, 6, 10.3389/fmars.2019.00055, 2019.
Hibler , W.: A Dynamic Thermodynamic Sea Ice Model, Journal of Physical Oceanography, 9, 815-846, 10.1175/1520-0485(1979)009<0815:adtsim>2.0.co;2, 1979.
Kaleschke, L., Lüpkes, C., Vihma, T., Haarpaintner, J., Bochert, A., Hartmann, J., and Heygster, G.: SSM/I Sea Ice Remote Sensing for Mesoscale Ocean-Atmosphere Interaction Analysis, Canadian Journal of Remote Sensing, 27, 526-537, 10.1080/07038992.2001.10854892, 2001.
Kalnay, E., Kanamitsu, M., Kistler, R., Collins, W., Deaven, D., Gandin, L., Iredell, M., Saha, S., White, G., Woollen, J., Zhu, Y., Chelliah, M., Ebisuzaki, W., Higgins, W., Janowiak, J., Mo, K. C., Ropelewski, C., Wang, J., Leetmaa, A., Reynolds, R., Jenne, R., and Joseph, D.: The NCEP/NCAR 40-Year Reanalysis Project, Bulletin of the American Meteorological Society, 77, 437-472, 10.1175/1520-0477(1996)077<0437:tnyrp>2.0.co;2, 1996.
Kauker, F., Kaminski, T., Karcher, M., Giering, R., Gerdes, R., and Voßbeck, M.: Adjoint analysis of the 2007 all time Arctic sea-ice minimum, Geophysical Research Letters, 36, 10.1029/2008gl036323, 2009.
Koldunov, N. V., Köhl, A., and Stammer, D.: Properties of adjoint sea ice sensitivities to atmospheric forcing and implications for the causes of the long term trend of Arctic sea ice, Climate dynamics, 41, 227-241, 2013.
Koldunov, N. V., Köhl, A., Serra, N., and Stammer, D.: Sea ice assimilation into a coupled ocean–sea ice model using its adjoint, The Cryosphere, 11, 2265-2281, 10.5194/tc-11-2265-2017, 2017.
Kwok, R.: Arctic sea ice thickness, volume, and multiyear ice coverage: losses and coupled variability (1958–2018), Environmental Research Letters, 13, 105005, 10.1088/1748-9326/aae3ec, 2018.
Large, W. G., McWilliams, J. C., and Doney, S. C.: Oceanic vertical mixing: A review and a model with a nonlocal boundary layer parameterization, Reviews of Geophysics, 32, 363-403, 1994.
Lavergne, T., Sørensen, A. M., Kern, S., Tonboe, R., Notz, D., Aaboe, S., Bell, L., Dybkjær, G., Eastwood, S., Gabarro, C., Heygster, G., Killie, M. A., Brandt Kreiner, M., Lavelle, J., Saldo, R., Sandven, S., and Pedersen, L. T.: Version 2 of the EUMETSAT OSI SAF and ESA CCI sea-ice concentration climate data records, The Cryosphere, 13, 49-78, 10.5194/tc-13-49-2019, 2019.
Losch, M., Menemenlis, D., Campin, J.-M., Heimbach, P., and Hill, C.: On the formulation of sea-ice models. Part 1: Effects of different solver implementations and parameterizations, Ocean Modelling, 33, 129-144, 2010.
Lyu, G., Koehl, A., Serra, N., and Stammer, D.: Assessing the current and future Arctic Ocean observing system with observing system simulating experiments, Quarterly Journal of the Royal Meteorological Society, 147, 2670-2690, https://doi.org/10.1002/qj.4044, 2021a.

https://doi.org/10.5194/egusphere-2022-1099
Preprint. Discussion started: 18 October 2022

Lyu, G., Koehl, A., Serra, N., Stammer, D., and Xie, J.: Arctic ocean–sea ice reanalysis for the period 2007–2016 using the adjoint method, Quarterly Journal of the Royal Meteorological Society, 147, 1908-1929, https://doi.org/10.1002/qj.4002, 2021b.
Ma, X., Mu, M., Dai, G., Han, Z., Li, C., and Jiang, Z.: Influence of Arctic Sea Ice Concentration on Extended-Range Prediction of Strong and Long-Lasting Ural Blocking Events in Winter, Journal of Geophysical Research: Atmospheres, 127, e2021JD036282, https://doi.org/10.1029/2021JD036282, 2022.
Marshall, J., Adcroft, A., Hill, C., Perelman, L., and Heisey, C.: A finite‐volume, incompressible Navier Stokes model for studies of the ocean on parallel computers, Journal of Geophysical Research: Oceans, 102, 5753-5766, 1997.
Maykut, G. A. and McPhee, M. G.: Solar heating of the Arctic mixed layer, Journal of Geophysical Research: Oceans, 100, 24691-24703, 10.1029/95jc02554, 1995.
Mazloff, M. R., Heimbach, P., and Wunsch, C.: An Eddy-Permitting Southern Ocean State Estimate, Journal of Physical Oceanography, 40, 880-899, 10.1175/2009jpo4236.1, 2010.
Morison, J., Wahr, J., Kwok, R., and Peralta‐Ferriz, C.: Recent trends in Arctic Ocean mass distribution revealed by GRACE, Geophysical Research Letters, 34, 2007.
Nguyen, A. T., Pillar, H., Ocaña, V., Bigdeli, A., Smith, T. A., and Heimbach, P.: The Arctic Subpolar Gyre sTate Estimate: Description and Assessment of a Data-Constrained, Dynamically Consistent Ocean-Sea Ice Estimate for 2002–2017, Journal of Advances in Modeling Earth Systems, 13, e2020MS002398, https://doi.org/10.1029/2020MS002398, 2021.
Overland, J. E., Ballinger, T. J., Cohen, J., Francis, J. A., Hanna, E., Jaiser, R., Kim, B. M., Kim, S. J., Ukita, J., Vihma, T., Wang, M., and Zhang, X.: How do intermittency and simultaneous processes obfuscate the Arctic influence on midlatitude winter extreme weather events?, Environmental Research Letters, 16, 043002, 10.1088/1748-9326/abdb5d, 2021.
Piecuch, C. G. and Ponte, R. M.: Importance of Circulation Changes to Atlantic Heat Storage Rates on Seasonal and Interannual Time Scales, Journal of Climate, 25, 350-362, 10.1175/jcli-d-11-00123.1, 2012.
Polyakov, I. V., Pnyushkov, A. V., Alkire, M. B., Ashik, I. M., Baumann, T. M., Carmack, E. C., Goszczko, I., Guthrie, J., Ivanov, V. V., Kanzow, T., Krishfield, R., Kwok, R., Sundfjord, A., Morison, J., Rember, R., and Yulin, A.: Greater role for Atlantic inflows on sea-ice loss in the Eurasian Basin of the Arctic Ocean, Science, 356, 285-291, 10.1126/science.aai8204, 2017.
Proshutinsky, A., Krishfield, R., Timmermans, M.-L., Toole, J., Carmack, E., McLaughlin, F., Williams, W. J., Zimmermann, S., Itoh, M., and Shimada, K.: Beaufort Gyre freshwater reservoir: State and variability from observations, Journal of Geophysical Research: Oceans, 114, 10.1029/2008jc005104, 2009.
Proshutinsky, A., Krishfield, R., Toole, J. M., Timmermans, M.-L., Williams, W., Zimmermann, S., Yamamoto-Kawai, M., Armitage, T. W. K., Dukhovskoy, D., Golubeva, E., Manucharyan, G. E., Platov, G., Watanabe, E., Kikuchi, T., Nishino, S., Itoh, M., Kang, S.-H., Cho, K.-H., Tateyama, K., and Zhao, J.: Analysis of the Beaufort Gyre Freshwater Content in 2003–2018, Journal of Geophysical Research: Oceans, 124, 9658-9689, 10.1029/2019jc015281, 2019.
Quadfasel, D., SY, A., WELLS, D., and TUNIK, A.: Warming in the Arctic, Nature, 350, 385, 1991.
Ricker, R., Hendricks, S., Kaleschke, L., Tian-Kunze, X., King, J., and Haas, C.: A weekly Arctic sea-ice thickness data record from merged CryoSat-2 and SMOS satellite data, The Cryosphere, 11, 1607-1623, 10.5194/tc-11-1607-2017, 2017.
Schauer, U., Beszczynska-Möller, A., Walczowski, W., Fahrbach, E., Piechura, J., and Hansen, E.: Variation of measured heat flow through the Fram Strait between 1997 and 2006, in: Arctic–Subarctic Ocean Fluxes, Springer, 65-85, 2008.
Serra, N., Käse, R. H., Köhl, A., Stammer, D., and Quadfasel, D.: On the low-frequency phase relation between the Denmark Strait and the Faroe-Bank Channel overflows, Tellus A: Dynamic Meteorology and Oceanography, 62, 530-550, 10.1111/j.1600-0870.2009.00445.x, 2010.
Smith, W. H. F. and Sandwell, D. T.: Global Sea Floor Topography from Satellite Altimetry and Ship Depth Soundings, Science, 277, 1956-1962, 10.1126/science.277.5334.1956, 1997.
Spreen, G., Kaleschke, L., and Heygster, G.: Sea ice remote sensing using AMSR-E 89-GHz channels, Journal of Geophysical Research: Oceans, 113, 10.1029/2005jc003384, 2008.
Stammer, D., Wunsch, C., Giering, R., Eckert, C., Heimbach, P., Marotzke, J., Adcroft, A., Hill, C. N., and Marshall, J.: Global ocean circulation during 1992–1997, estimated from ocean observations and a general circulation model, Journal of Geophysical Research: Oceans, 107, 1-1-1-27, https://doi.org/10.1029/2001JC000888, 2002.

https://doi.org/10.5194/egusphere-2022-1099
Preprint. Discussion started: 18 October 2022

577 Tilling, R. L., Ridout, A., and Shepherd, A.: Estimating Arctic sea ice thickness and volume using CryoSat-2 radar
578 altimeter data, Advances in Space Research, 62, 1203-1225, https://doi.org/10.1016/j.asr.2017.10.051, 2018.
579 Toole, J.M., Krishfield, R., Woods Hole Oceanographic Institution Ice-Tethered Profiler Program, Ice-Tethered
580 Profiler observations: Vertical profiles of temperature, salinity, oxygen, and ocean velocity from an Ice-Tethered
581 Profiler buoy system. NOAA National Centers for Environmental Information. Dataset.
582 https://doi.org/10.7289/v5mw2f7x, 2016.
583 Toyoda, T., Hirose, N., Urakawa, L. S., Tsujino, H., Nakano, H., Usui, N., Fujii, Y., Sakamoto, K., and Yamanaka,
584 G.: Effects of Inclusion of Adjoint Sea Ice Rheology on Backward Sensitivity Evolution Examined Using an Adjoint
585 Ocean–Sea Ice Model, Monthly Weather Review, 147, 2145-2162, 10.1175/mwr-d-18-0198.1, 2019.
586 Uotila, P., Goosse, H., Haines, K., Chevallier, M., Barthélemy, A., Bricaud, C., Carton, J., Fučkar, N., Garric, G.,
587 Iovino, D., Kauker, F., Korhonen, M., Lien, V. S., Marnela, M., Massonnet, F., Mignac, D., Peterson, K. A.,
588 Sadikni, R., Shi, L., Tietsche, S., Toyoda, T., Xie, J., and Zhang, Z.: An assessment of ten ocean reanalyses in the
589 polar regions, Climate Dynamics, 52, 1613-1650, 10.1007/s00382-018-4242-z, 2019.
590 Woodgate, R. A., Weingartner, T. J., and Lindsay, R.: Observed increases in Bering Strait oceanic fluxes from the
591 Pacific to the Arctic from 2001 to 2011 and their impacts on the Arctic Ocean water column, Geophysical Research
592 Letters, 39, 2012.
593 Wunsch, C. and Heimbach, P.: Practical global oceanic state estimation, Physica D: Nonlinear Phenomena, 230,
594 197-208, https://doi.org/10.1016/j.physd.2006.09.040, 2007.
595 Yang, C.-Y., Liu, J., and Xu, S.: Seasonal Arctic Sea Ice Prediction Using a Newly Developed Fully Coupled
596 Regional Model With the Assimilation of Satellite Sea Ice Observations, Journal of Advances in Modeling Earth
597 Systems, 12, e2019MS001938, https://doi.org/10.1029/2019MS001938, 2020.
598 Zhang, J. and Hibler III, W.: On an efficient numerical method for modeling sea ice dynamics, Journal of
599 Geophysical Research: Oceans, 102, 8691-8702, 1997.
600 Zhang, J. and Rothrock, D. A.: Modeling Arctic sea ice with an efficient plastic solution, Journal of Geophysical
601 Research: Oceans, 105, 3325-3338, 2000.
602 Zweng, M. M., Reagan, J. R., Seidov, D., Boyer, T. P., Locarnini, R. A., Garcia, H. E., Mishonov, A. V., Baranova,
603 O. K., Weathers, K. W., Paver, C. R., and V, S. I.: World Ocean Atlas 2018, Volume 2: Salinity S, Levitus, edited
604 by: Mishonov, A., NOAA Atlas NESDIS, 82, 50, 2018.
605